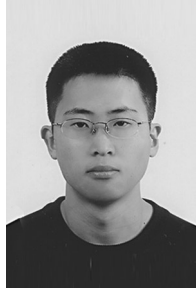


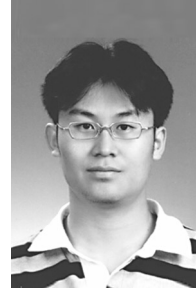
New Far-Field Boundary and Initial Conditions for Computation of Rotors in Vertical Flight Using Vortex Tube Model



Wooyoung Choi*
Graduate Research Assistant



Seunghoon Lee
Graduate Research Assistant



Jiyoung Jung
Graduate Research Assistant



Soogab Lee
Professor

Aeroacoustic & Noise Control Laboratory, Seoul National University, Seoul, Korea

Motivated by demands for improved far-field boundary condition and initial condition for computations of helicopter rotor aerodynamics, a theoretical model using a truncated vortex tube concept is applied to the Navier–Stokes computations. A helicopter rotor wake is represented by the truncated vortex tube of continuously distributed vorticity in this model. Velocity components induced by the vortex tube are used to specify the far-field boundary and initial conditions. Computations were done for the UH-60A model-rotor test cases in hover. The results of the vortex tube model boundary condition show good agreements with the measured performance values and provide a more accurate prediction of rotor wake than that of the source-sink boundary condition. In addition, the initial condition using the vortex tube model enables faster convergence and gives more stable solutions than an initial condition assuming quiescent flow fields. Its application is also easily extended to climbing/descending flights, because the vortex tube model was originally devised to calculate induced flows of a helicopter rotor in the vertical flight. Computed rotor performance values agree with experimental results for various vertical flight conditions. The overall results show that the vortex tube model can be used for the new far-field boundary condition and initial condition when performing helicopter rotor analysis.

Nomenclature

A'	amplification factor
c	chord length
C_T	thrust coefficient, $= \frac{T}{1/2\rho\pi R^2 V_{tip}^2}$
C_Q	torque coefficient, $= \frac{T}{1/2\rho\pi R^3 V_{tip}^2}$
d	distance from a rotor hub
H	truncated vortex tube length, m
\bar{H}	normalized truncated vortex tube length, $= H/R$
k_H	transport distance factor
k'_i	transport velocity factor
M_{tip}	rotor tip Mach number
\vec{p}	arbitrary position vector
R	rotor radius, m
r	radial distance from rotor hub, m
Re	Reynolds number
$V_{i,hover}$	Induced velocity in hover, m/s
V_i	total transport velocities of trailing vortices, m/s
\bar{V}_i	normalized wake transport velocity, $= V_i/V_{i,hover}$
V_{tip}	rotor tip velocity, m/s
V_v	rotor upward axial velocity, m/s
\bar{V}_v	normalized rotor upward axial velocity, $= V_v/V_{i,hover}$
v_r	radial induced velocity, m/s
\bar{v}_r	normalized radial induced velocity, $= v_r/V_{i,hover}$
v_z	axial induced velocity, m/s
\bar{v}_z	normalized axial induced velocity, $= v_z/V_{i,hover}$

W_{in}	inflow velocity at far-field boundaries, m/s
W_{out}	outflow velocity at far-field boundaries, m/s
x	coordinate direction along the rotor chord, m
y	coordinate direction along the rotor span, m
z	coordinate direction normal to the rotor disk, m
θ	rotor collective pitch angle, deg
ϕ	azimuth angle, rad
Γ	circulation per unit length of the truncated vortex tube

Introduction

Prediction of the rotor wake has been an important issue in the area of aerodynamic design and analysis of helicopter rotor blades. It is a principal consideration in the predictions of rotor loads, performance, and acoustics. However, the prediction of the rotor wake has been one of the most challenging problems in computational fluid dynamics (CFD). One of the key problems is reducing numerical dissipation that would enable accurate prediction of rotor tip vortices. Over the past few years, various research projects have been performed to overcome the shortcomings related to the dissipation. With respect to the commonly used CFD methods, which are based on the Euler or Navier–Stokes equations, the accuracy of capturing vortices could be improved by modifying the grid system or numerical schemes. So, some research efforts have focused on the grid system, for example, unstructured grid (Ref. 1), chimera grid (Ref. 2), and adaptive grid techniques (Ref. 3). The numerical schemes have been developed as well. In one such study Hariharan and Sankar (Ref. 4) used a high-order spatial discretization scheme for a hovering rotor, whereas Usta and others adapted weighted essentially nonoscillatory (WENO) scheme to improve the accuracy of tip vortex prediction (Refs. 5,6). Wenren and Steinhoff (Ref. 7) proposed the vorticity

*Corresponding author; email: yanni1@snu.ac.kr.

Presented at the American Helicopter Society International Specialists' Meeting, Seoul, Korea, October 15–17, 2007. Received August 2007; accepted July 2008.

confinement method, which regulates the vorticity of tip vortex during calculation. It showed relatively good conservation of tip vortices in spite of the numerical dissipation.

Some researchers have proposed unique concepts of calculating the tip vortices instead of improving CFD schemes or grids themselves. Sankar and coworkers (Ref. 8) suggested the hybrid method, combining CFD and the free wake model. In the hybrid method, CFD is applied around the rotor to calculate blade loads, and the free wake model is used to compute rotor wake. Recently, Brown (Ref. 9) developed the VTM (vorticity transport model), which is based on the vorticity transport equations. The VTM showed good performance, suggesting a possibility of using it for the prediction in various flight conditions.

Another existing problem is being able to specify far-field boundary conditions for computation of a hovering rotor. In the case of hovering or descending flight, the rotor tip vortices usually do not quickly pass away. Moreover, they are located very near to a rotor blade, causing it to have a strong influence on the overall performance and complex flow around a rotor. The most ideal condition is to adopt a sufficiently large computational domain without allowing inflow or outflow at the boundaries. If we assume the quiescent flow outside of the computational box, then the flow into and out of the box will be zero. This creates a closed box environment for the rotor, and the flow inside the box recirculates when the rotor is spinning. In principle, this is precisely the environment found in many hover test chambers (Ref. 10). However, such a large computational box requires much computation time and cost. If a smaller computation box is adopted for computational cost and efficiency, a nonzero flow far-field boundary should be specified, which allows inflow and outflow at the boundaries without violating the mass conservation law.

Most of the previous hovering rotor calculations have used the point/sink momentum theory characteristic boundary condition (Refs. 10–14). This boundary condition is usually called the source-sink far-field boundary condition (Refs. 10,11) or the Froude condition (Refs. 15,16). This model determines the outflow at the far-field boundary using the one-dimensional (1D) momentum theory. Then, it assumes that a point sink is placed at the center of the rotor hub to specify the inflow into the computational domain to satisfy the mass conservation law. Many previous researches have shown that the source-sink model has a good convergence characteristic and is able to predict the overall performance well. Brian and Baeder (Ref. 12) performed extensive Navier–Stokes computations for a hovering rotor using the source-sink model. Although reasonable agreements were obtained between the computed performance and the experimental data (Ref. 13), the computed value of the velocity at the bottom outflow boundary was much lower than it was expected. In addition, their computations showed rather poor predictions of tip vortex geometry. The tip vortex passing above a rotor blade or the tip vortex collision against a following rotor blade is occasionally observed in the computation of high-thrust condition. It is a completely nonphysical phenomenon. These disagreements may result from the lack of the grid resolution by today's standards. Other recent research using the boundary condition still, however, has shown a similar problem in the prediction of the rotor tip vortex (Refs. 14,15). Computations of rotor wake geometry, such as vertical descent and radial contraction, did not show good agreement with the experimental data even after half a revolution. The tip vortex generated by preceding blade passed the following blade more closely in computation than in the experimental result. This causes a chronic problem in rotor simulations—an overprediction of the sectional thrust near the rotor tip compared to the experimental data.

Although the simplicity of the source-sink model is a primary factor for its wide use in the hovering analysis, it has some inherent vulnerable points and limitations. As rotor wake travels downstream, the strength of rotor downwash decreases and the radius of downstream area increases

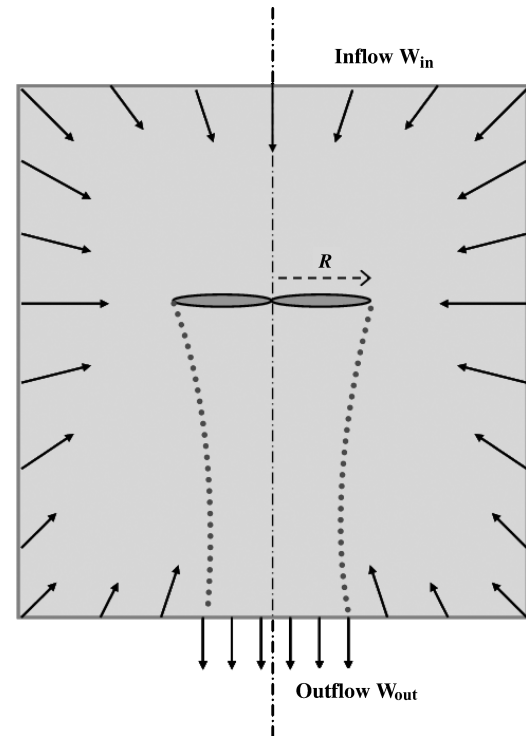


Fig. 1. Source-sink model schematic.

in general. Thus, it is reasonable that the size of outflow region and velocity components at the bottom far-field boundary should be changed according to the size of computational domain. However, the outflow boundary condition in the source-sink model is not varied regardless of the far-field boundary location. Moreover, it is debatable to set the direction of inflow velocity toward the rotor hub at all far-field boundaries except the outflow region below the rotor disk, as shown in Fig. 1. Finally, the applications of the source-sink model are limited to only hovering analysis because of its assumption (Ref. 10).

Wang (Ref. 17) proposed an analytic model for calculating the mean-induced flow through the rotor disk in axial flight. This model is based on the simplifying assumptions about the nature of the mean flow through the rotor, leading to a simple representation of the mean rotor wake by a truncated vortex tube of continuously distributed vorticity (Ref. 18). This model shows good agreement with the experimental results of the timewise-mean-induced velocity averaged over the rotor disk area, for a wide range of descent rates, including vortex ring and turbulent wake flow.

In this research, the truncated vortex tube model was implemented in a three-dimensional Navier–Stokes flow solver used in the simulation of rotor wakes. The use of the truncated vortex tube model has some strong points for the far-field boundary and initial conditions, because the entire flow field around a rotor is computed using the vortex tube model, which is similar to real flow fields. Therefore, it is expected that a new far-field boundary condition using the truncated vortex tube induced flow is physically more reasonable than the conventional boundary condition. Computed flow properties inside of the computational domain can also be useful to assume an initial condition. Starting from the initial condition would accelerate convergence as compared to a quiescent flow initial condition. Moreover, application of the truncated vortex tube model is not confined to the analysis of hovering flight, but is extended to the analysis of vertical flight.

These favorable characteristics of the truncated vortex tube model in the rotor wake modeling were confirmed by comparisons with several validation cases. This paper deals with the flow analysis and the aerodynamic performance prediction mainly for the hovering flight condition, a brief analysis of climbing and descending flight is also covered. The primary purpose of this work is to analyze the possibility of new far-field boundary and initial conditions, using the truncated vortex tube model for the rotor analysis.

Numerical Method

Navier–Stokes flow solver

The HeliNA code developed by Aeroacoustic Noise Control Laboratory (AANCL) was used for all the computation of rotor flow. It is the three-dimensional Reynolds-averaged Navier–Stokes solver designed for the helicopter rotor computations. The Baldwin–Lomax turbulence model is used in this study. The Roe’s flux difference splitting scheme combined with the fifth-order WENO (Ref. 5) approach was applied for the higher order spatial accuracy, and the lower–upper symmetric Gauss–Seidel (LU-SGS) method (Ref. 19) was adopted to perform the temporal integration. In the case of helicopter axial flight, there are some useful characteristics that reduce the computational burden. Its flow field is steady state when it is observed from blade-fixed coordinates. So the source term formulation from Chen et al. (Ref. 20) is implemented in the governing equation instead of the moving rotor grid. Finally, the entire flow field is periodic, so the size of computational domain is reduced by the factor of 4 by using periodicity for a four-blade rotor hovering case.

Overset grid system

To minimize numerical dissipation of tip vortices, it is necessary to investigate effects of the boundary condition and initial condition on the rotor wake. An overset grid system was used to accurately capture tip vortices. The grid system is composed of one C–H type main rotor grid, three H–H type near-field grids to capture the tip vortex accurately, and one H–H type far-field grid, as shown in Fig. 2(a). The far-field grid has a quarter cylinder shape for a four-bladed rotor. The rotor grid is located in the center of the far-field grid. The quarter cylinder shaped near-field grid surrounds the rotor grid and covers the rotor wake region.

Grid overlaps have been used between adjacent grids to improve the accuracy of the flow information exchanges in the overset grid. The C–H grid on the rotor contains $161 \times 110 \times 45$ grids point in the chordwise, spanwise, and normal direction, as shown in Fig. 2(b). The H–H type near-field grid is divided into 14 blocks, and each block contains 0.8 million grid points. The number of far-field grid points is also 0.8 million. The total number of grid points is about 12.8 million. The solution was computed on a parallel machine.

To investigate the effect of the boundary condition, the same hovering computations were conducted for four different far-field boundary locations: $1.5R$, $2R$, $3R$, and $5R$. Each far-field grid is extended by exponential stretching. Far boundaries are located at 1.5, 2, 3, and 5 blade radii from the rotor hub in the axial and radial directions. For example, the $2R$ far-field boundary condition has a quarter cylinder shape with radius of 2 blade radii and height of 4 blade radii, as shown in Fig. 2(a).

Source-sink boundary condition

Srinivasan et al. (Ref. 10) proposed the source-sink boundary condition to prescribe the inflow and outflow at far-field boundaries, as

illustrated in Fig. 1. Rotor outflow that is far from the rotor can be easily calculated by the 1D momentum theory (or Froude theory) using the following equation:

$$W_{\text{out}} = -2V_{\text{tip}}\sqrt{C_T/2} \quad (1)$$

Although the downstream radius of the outflow is given by $R/\sqrt{2}$ according to the theory, the radius of this outflow boundary of the computational box is empirically set by $1.12R/\sqrt{2}$. The potential sink of mass is located at the center of rotor hub to draw the flow into the computational domain from all of the far-field boundaries except the outflow boundary. Outflow velocity calculated by the momentum theory is not used directly to prescribe outflow boundary condition. Instead, it determines the inflow velocity. Inflow strength is adjusted to satisfy mass conservation across the boundaries of computational domain. In other words, the total inflow rate at the far-field boundaries is equal to total outflow rate, which is estimated by Eq. (1). The inflow strength can be calculated by the following equations:

$$W_{\text{in}} = -\frac{V_{\text{tip}}}{4}\sqrt{\frac{C_T}{2}}\left(\frac{R}{d}\right)^2 \quad (2)$$

where V_{tip} is the rotor tip speed, C_T is the thrust coefficient, $d^2 = x^2 + y^2 + z^2$, and R is the rotor radius. The inflow is prescribed in the direction toward the rotor hub on all the boundaries.

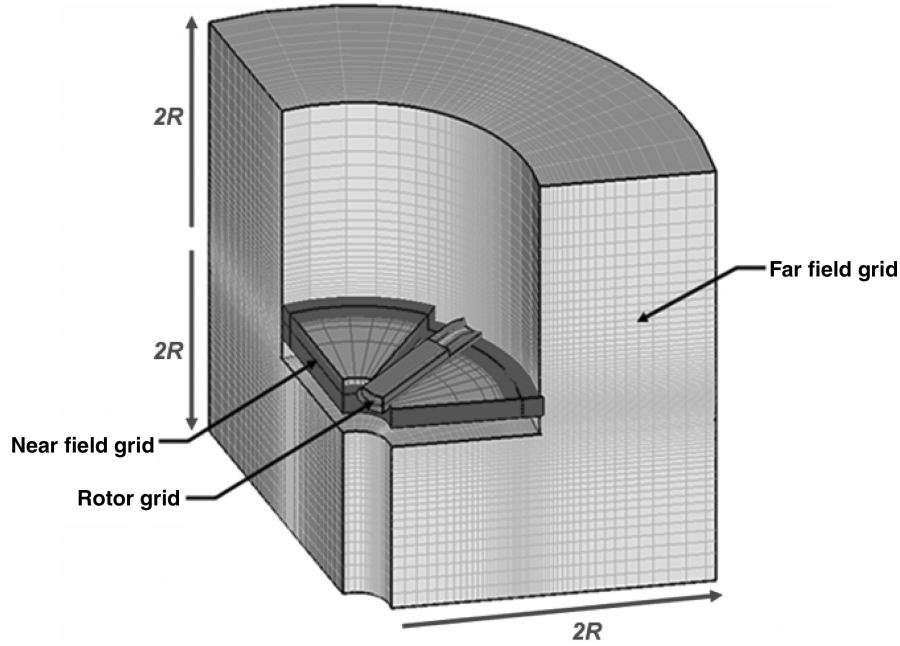
For the inflow boundary condition, density is fixed to the freestream value, and the three components of velocity are computed by Eq. (2). The isentropic relation between freestream and boundary flow field can determine density and pressure at the inflow boundary. These inflow boundary values are then combined with the values from the flow field interior by prescribing the external entropy, tangential velocity, incoming Riemann invariant, and extrapolating the outgoing Riemann invariant from the interior (Ref. 14). In contrast, pressure is fixed to the freestream value, and the other properties, density and three velocity components, are extrapolated from the interior for the outflow boundary condition. As a result, the mass outflow automatically compensates for the mass inflow.

Truncated vortex tube model boundary condition

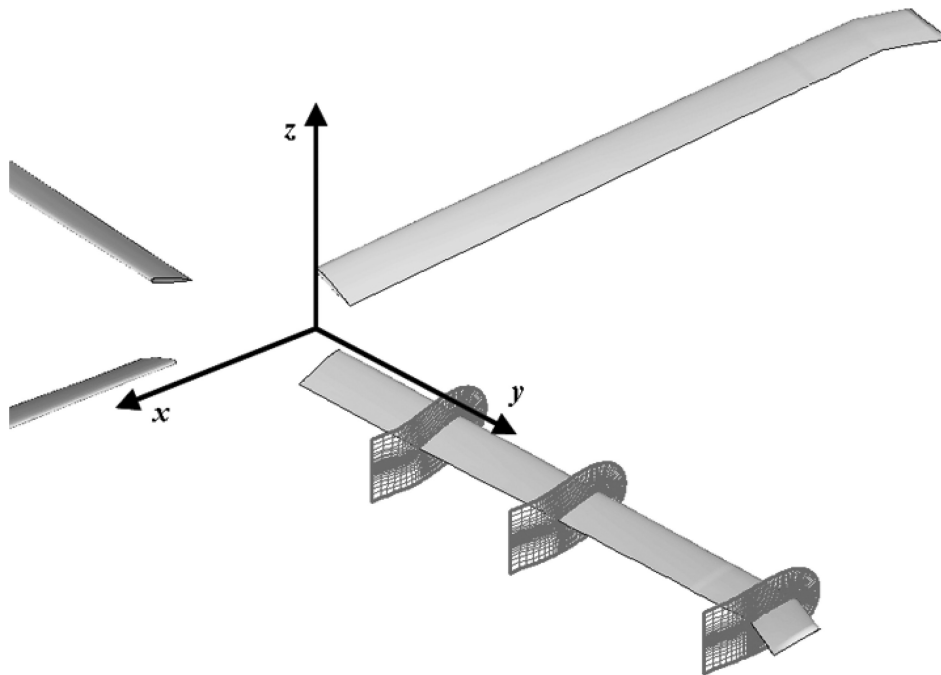
The truncated vortex tube model (Ref. 17) was devised to calculate the induced velocity through the rotor disk in axial flight. This is the first step beyond the disk momentum theory, incorporating some sense of the rotor wake as a vortical system (Ref. 18). This model considers a rotor wake as a constant radius tube of continuous distributed vorticity aligned with the tube circumference with an axial spatial density, as shown in Fig. 3. The height of truncated vortex tube is H and its radius is R . This truncated vortex tube generates a large circulating flow, which goes through the rotor disk at the top of the vortex tube and comes out through the bottom of vortex tube. Let there be an infinitesimal vortex element located at a point $\vec{s} = (R \cos \phi, R \sin \phi, z)$ on the vortex tube surface. Its strength is Γ per unit length circumferentially and axially down the vortex tube. According to the Biot–Savart law, the element $\Gamma d\vec{s}$ produces an induced velocity $d\vec{v}$ at an arbitrary observer point $\vec{p} = (x_p, y_p, z_p)$. Integrating along azimuthal and axial directions for the entire truncated vortex tube, the induced velocity can be expressed in the following vector form:

$$\vec{v}(p) = \iint \frac{\Gamma dz d\vec{s} \times \vec{d}}{4\pi |\vec{d}|^3} \quad (3)$$

where $\vec{d} = \vec{p} - \vec{s}$ and $d\vec{s} = -R \sin \phi d\phi \hat{i} + R \cos \phi d\phi \hat{j}$.



(a) Overset grid schematics (2R far-field boundary condition)



(b) Rotor grid system and xyz coordinates

Fig. 2. Overset grid schematic.

Wang assumes that vortex strength, Γ , decays linearly to zero along the wake. Vortex strength Γ is calculated from the thrust coefficient as follows:

$$\Gamma(z) = \Gamma_0 \left(1 - \frac{y}{H}\right) = -2 \frac{v_{i,hov}}{\bar{V}_t} \left(1 - \frac{y}{H}\right) \quad (4)$$

where $V_{i,hov} = -V_{tip} \sqrt{C_T/2}$ is the hovering induced velocity of the rotor and \bar{V}_t is the normalized wake transport velocity (Ref. 21).

According to Wang's study, normalized rotor axial velocity is a function of normalized truncated vortex tube length \bar{H} and several parameters

are as follows:

$$\bar{V}_v = \frac{\bar{H}}{k_H} + \frac{k_H k'_t A'}{2\bar{H}^2} (\sqrt{\bar{H}^2 + 1} - 1) \quad (5)$$

$$\bar{H} = k_H \bar{V}_t \quad (6)$$

Thus, truncated vortex tube length \bar{H} in some axial flight conditions could be estimated by using the iterative method such as the Newton-Raphson method. Normalized truncated vortex tube length \bar{H} is assumed to be proportional to the normalized wake transport velocity \bar{V}_t . These parameters k_H , k'_t , and A' in Eqs. (5) and (6) are determined empirically

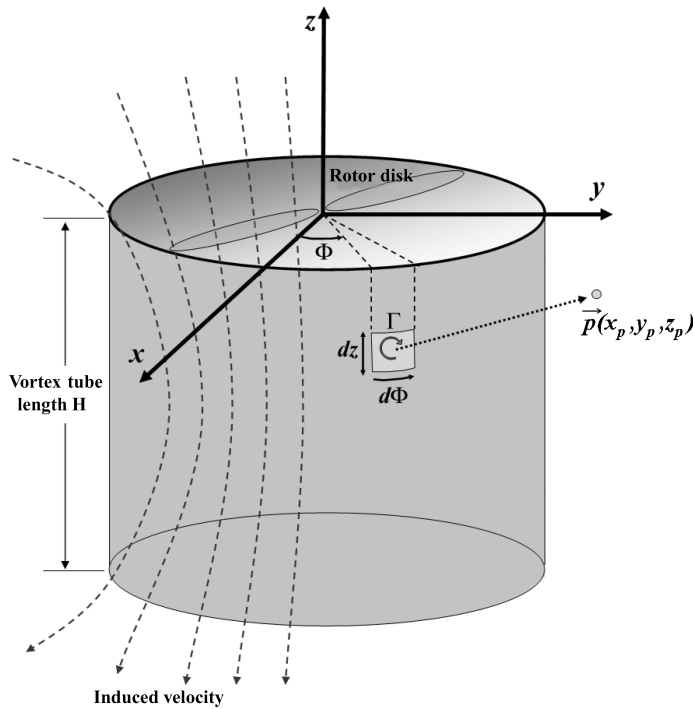


Fig. 3. Truncated vortex tube model schematic.

from the experimental results. Given optimal values are as follow:

$$k_H = -3, \quad A' = 1.62, \quad k'_t = 2 - 0.8 \exp \left[- \left(\frac{\bar{H}}{2} \right)^2 \right] \quad (7)$$

Because the induced flow computed by Eq. (3) had axial symmetry, the induced velocity vector could be decomposed into radial velocity and axial velocity components. All the velocity components are normalized by the hovering induced velocity and all the length units are normalized by the rotor radius R . Finally, integrating along azimuthal and axial directions for the entire vortex tube, the normalized induced radial velocity \bar{v}_r , and axial velocity \bar{v}_z at an arbitrary point \bar{p} can be expressed by the following equations (Ref. 18):

$$\bar{v}_r(\bar{p}) = - \int_0^{\bar{H}} \int_0^{2\pi} \frac{1}{2\pi \bar{V}_t} \frac{(1 - \frac{\bar{z}}{\bar{H}}) [(\bar{z}_p - \bar{z}) \cos \phi]}{[\bar{x}_p^2 + 1 - 2\bar{x}_p \cos \phi + (\bar{z}_p - \bar{z})^2]^{3/2}} d\phi d\bar{z} \quad (8)$$

$$\bar{v}_z(\bar{p}) = - \int_0^{\bar{H}} \int_0^{2\pi} \frac{1}{2\pi \bar{V}_t} \frac{(1 - \frac{\bar{z}}{\bar{H}}) [1 - \bar{x}_p \cos \phi]}{[\bar{x}_p^2 + 1 - 2\bar{x}_p \cos \phi + (\bar{z}_p - \bar{z})^2]^{3/2}} d\phi d\bar{z} \quad (9)$$

Normalized induced velocity solutions for the entire flow fields can be computed by numerical integration of Eqs. (8) and (9).

The key idea of the vortex tube model boundary condition is to specify the far-field boundary conditions, using these velocity components induced by the vortex tube model. In the source-sink boundary condition, the mass conservation of the computational domain is only consideration to estimate the velocity components of inflow and outflow at far-field boundaries. Since the inflow direction is fixed to the rotor hub in all direction and inflow strength is simply in an inverse proportion to the distance from the rotor hub, this boundary condition could not reflect rotor flow fields inside the computational domain. In the vortex tube model boundary condition, the inflow or outflow velocity components are extracted from the entire flow fields induced by the vortex tube, which is changed according to the overall thrust. Therefore, it is expected that the vortex

tube model boundary condition is physically more reasonable to simulate rotor flow fields compared to the source-sink boundary condition.

Although the numerical integration of Eqs. (8) and (9) can be somewhat troublesome, normalized induced velocity components at the far-field boundaries are calculated just once at the first stage of computation. These velocity components are multiplied by $V_{i,hover}$ and applied to the far-field boundary condition at every time step. Since the computed thrust varies during iteration process, the inflow and outflow conditions at the far-field boundary are continuously changed from time to time. The signs of these inflow velocities determine the inflow/outflow characteristic boundary condition based on the one-dimensional Riemann invariants that should be used. For the inflow boundary, density and pressure can be calculated by using the isentropic relation between the boundary fields and the stagnation flow at infinity (Ref. 14). Three velocity components of the inflow are specified by the computed result of Eqs. (8) and (9), and combined with values from the flow field interior by prescribing the external entropy, tangential velocity, and Riemann invariants. For the outflow boundary, the freestream pressure is prescribed, and all other quantities are extrapolated from the interior. The resulting mass outflow automatically is adjusted to match the inflow. Finally, all the calculated flow quantities are applied to the far-field boundary. The vortex tube model is expected to help the development of the rotor wake structure. Even after the rotor wake is fully developed in the computation, the vortex tube model boundary condition is still applied to the far-field boundary condition to specify the inflow velocity.

Initial condition using the truncated vortex tube model

In general, there is no information about the flow fields at an initial stage of computation. Thus, many hovering computations start from the initial condition that assumes that there is a quiescent flow field around a rotor. Since the entire flow field could be estimated based on the overall thrust using the truncated vortex tube model, these flow velocities can be used as an initial condition to accelerate convergence. Freestream properties are used for the initial density and pressure. The initial condition derived by the truncated vortex tube model was used and compared with the quiescent flow initial condition.

Results and Discussion

Truncated vortex tube model test case

Figure 4 presents flow fields induced by a truncated vortex tube for the various types of axial flight for a UH-60A rotor blade. All the flow fields are computed by the numerical integration of Eqs. (8) and (9) and not by the CFD simulation. The boundaries of the computational domain are located at 2 blade radii from the rotor blade tip. This reflects the actual positions of the computation box boundaries used for the CFD computation. For the hovering state in Fig. 4(a), the vortex tube generates a strong downwash below the rotor disk and a recirculating flow around the rotor wake. Figure 4(b) shows a flow field in slow climbing state, and Fig. 4(c) shows a flow field in slow descending flight state. Typical vortex ring flow is generated on a fast descent, as shown in Fig. 4(d). The length of the truncated vortex tube is a function of the axial velocity, as shown in Eqs. (5) and (6). Its length is about 3.2 radii for a hovering rotor in Fig. 4(a), and 3.84 radii for a climbing rotor in Fig. 4(b). On the contrary, the truncated vortex tube length decreases for a descending rotor and becomes almost zero for a vortex ring state as shown in Fig. 4(d).

Figure 5 shows the axial velocity distributions for the various vertical velocities at the bottom far-field boundary, which is located at 2 blade radii from the rotor disk. Inflow or outflow profiles at the bottom

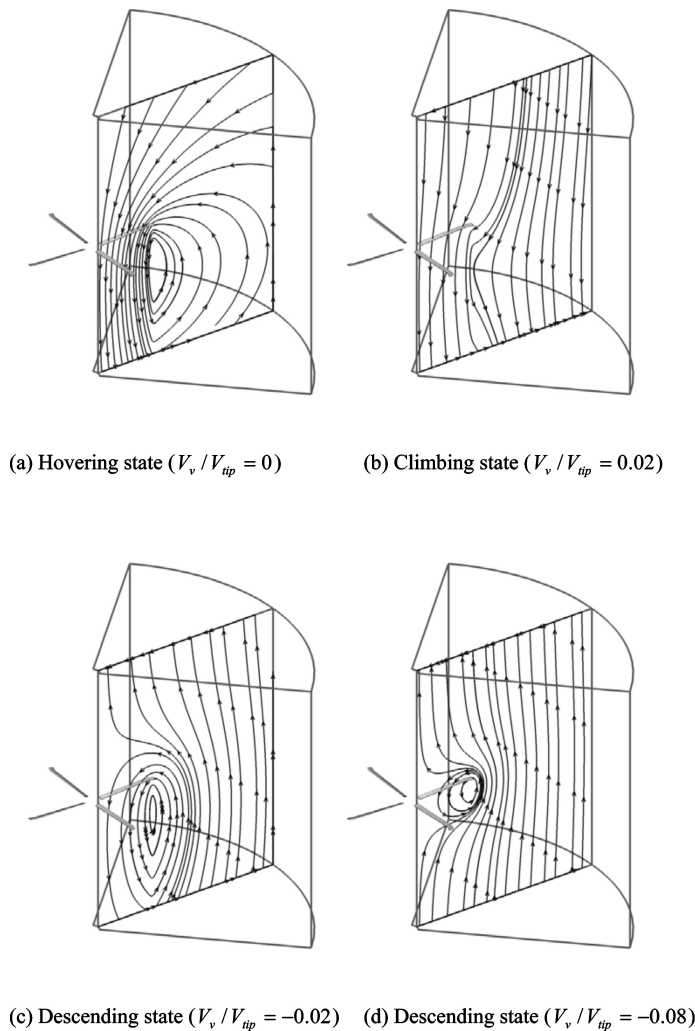


Fig. 4. Flow fields induced by a truncated vortex tube ($2R$ far-field boundary).

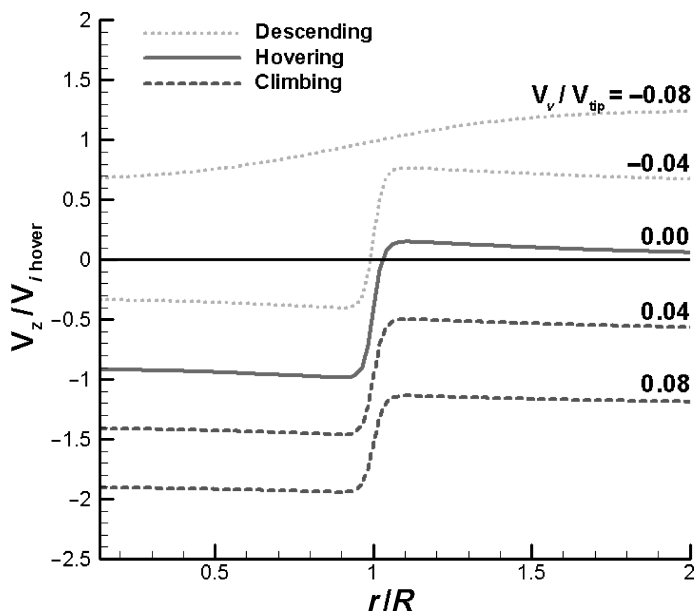


Fig. 5. Axial velocity distribution induced by a truncated vortex tube at $2R$ bottom far-field boundary for the various vertical velocities.

boundary vary according to rotor vertical velocities. In hover, the strength of downwash at a bottom boundary is almost same as the hover induced velocity, $V_{i,hov}$. The radius of outflow region in the truncated vortex tube model is generally larger than the specified outflow region in the source-sink model, and its radius is changed according to the axial velocity and the size of computational domain.

It should be noted that Fig. 4(a) shows both radial contraction and expansion of the rotor stream tube. The expansion of the rotor stream tube causes the expansion of the outflow region at the bottom boundary. The source-sink boundary condition only considers the radial contraction, which is caused by the acceleration of induced velocity through the stream tube; the radius of this stream tube is ideally assumed to be contracted from R at the rotor plane to $R/\sqrt{2}$ at the far wake region. Thus, the radius of the outflow region in the source-sink model is fixed at the far-field boundary regardless of the far boundary location. However, some previous experimental results showed that the rotor wake does not ideally contract as it moves downwardly (Refs. 22,23). After a few rotor revolutions, the induced velocity effect causes adjacent turns of the tip vortices, thus altering their descent velocities and resulting in “vortex-pairing” phenomenon and the complete merger of pairing vortices. It causes disturbances of the rotor wake structure and expansion of the rotor stream tube. Other studies using computations also showed similar expansion of rotor wake (Refs. 24–26). The expansion of stream tube in the result of the vortex tube model is quite reasonable when the effects of vortices interaction and viscous dissipation are considered,

As a result, the vortex tube model shows a general characteristic pattern of the entire flow fields for each axial flight. These results suggest the possibility for a new boundary condition and an initial condition. Thus, the truncated vortex tube model was implemented in the HeliNA code to specify far-field boundary conditions and initial condition. The truncated vortex tube model boundary condition uses only the boundary values of flow fields, and the truncated vortex tube model initial condition uses entire flow field information.

Computational result (UH-60A)

The hovering calculation was performed for the UH-60A model rotor and compared with the experimental data, which was tested by Lorber et al. (Ref. 13). All the cases were computed at the same tip

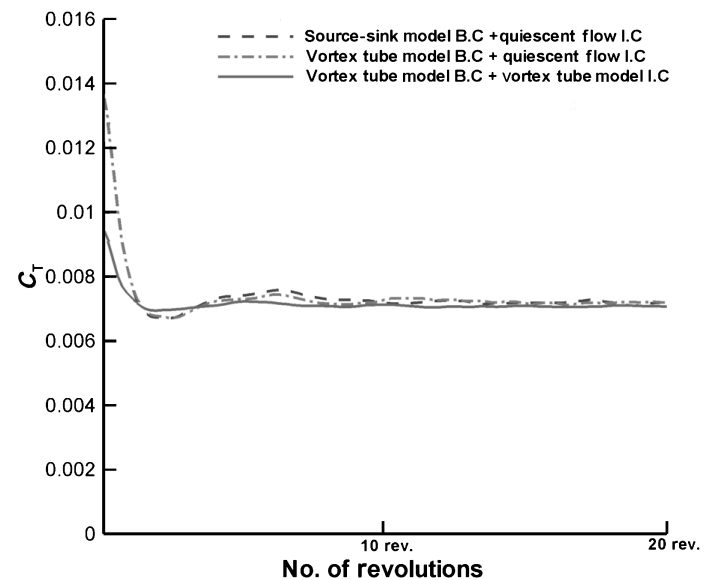
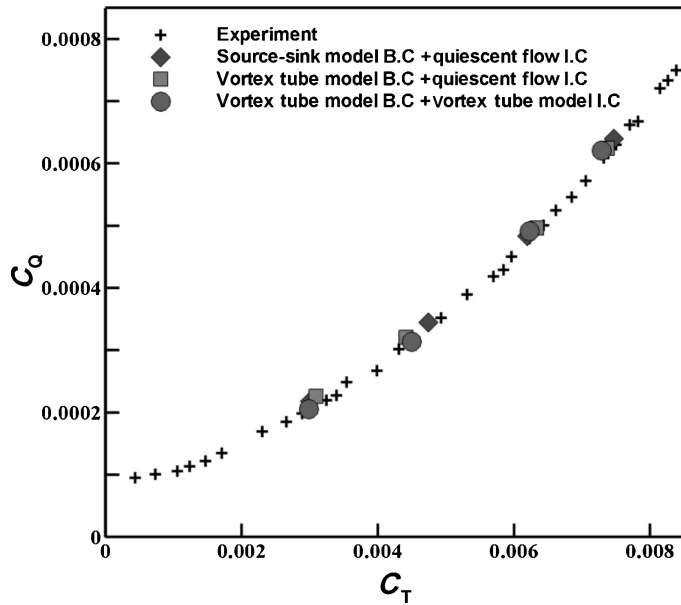
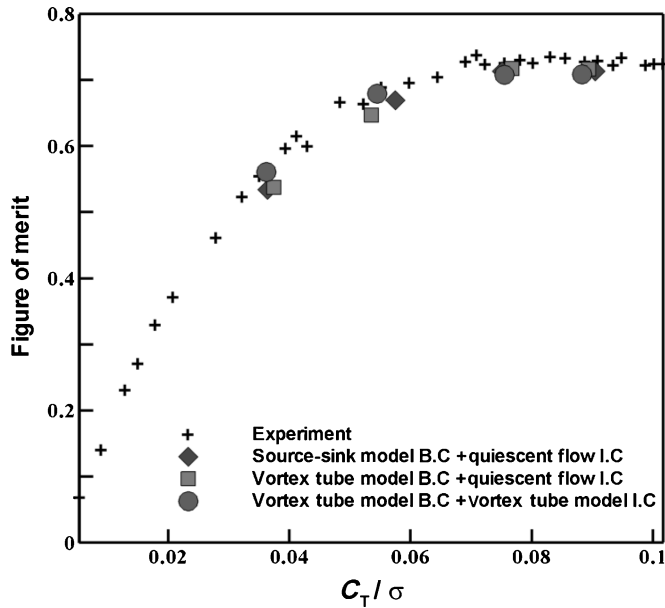


Fig. 6. Thrust convergence history for a hovering rotor.



(a) Thrust and power results



(b) C_T/ρ and figure of merit results

Fig. 7. Prediction of overall performance for the UH-60A model rotor ($M_{tip} = 0.628$).

Mach number 0.628 for comparison with the experimental data. To consider effects of rotor aeroelasticity, the rotor blade grid was generated including experimentally measured coning angle and elastic twist. All the computations were conducted under the following three test conditions: source-sink far-field boundary condition with the quiescent flow initial condition, truncated vortex tube model far-field boundary condition with the quiescent flow initial condition, and truncated vortex tube model far-field boundary condition with the truncated vortex tube model initial condition. The truncated vortex tube model is briefly referred to as a “vortex tube model” in the figures.

Figure 6 shows a C_T convergence history for a typical condition. All the hovering computations were conducted for 20 rotor revolutions,

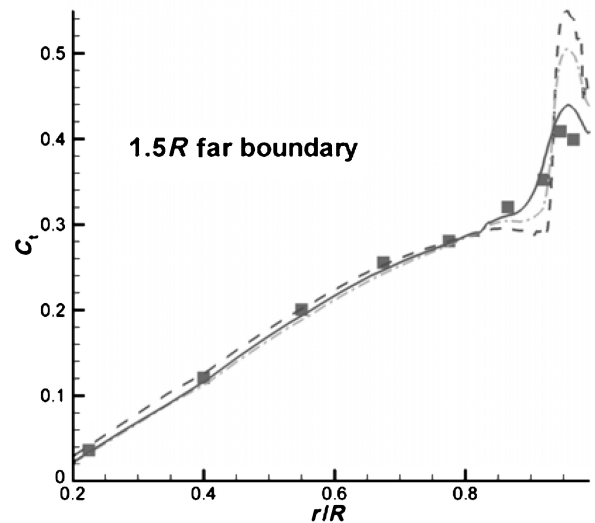
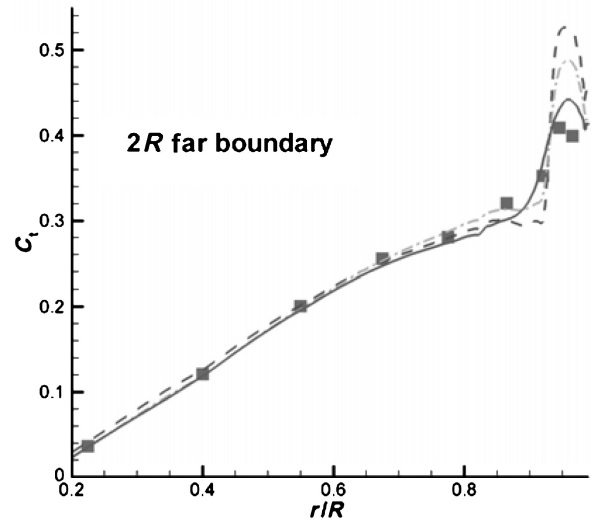
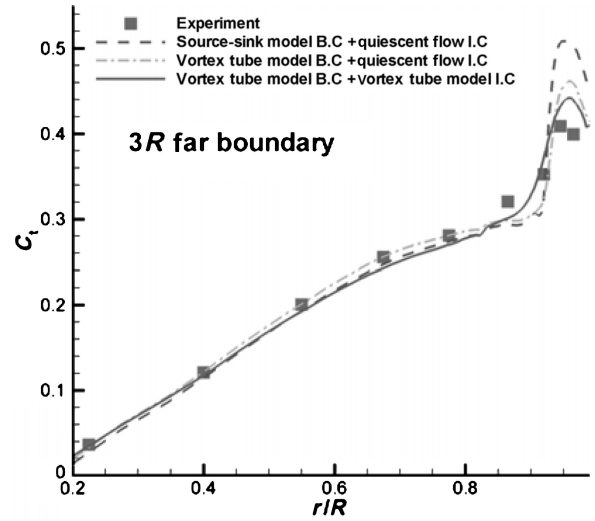


Fig. 8. Spanwise thrust distribution for hovering ($M_{tip} = 0.628$, $C_T = 0.00706$).

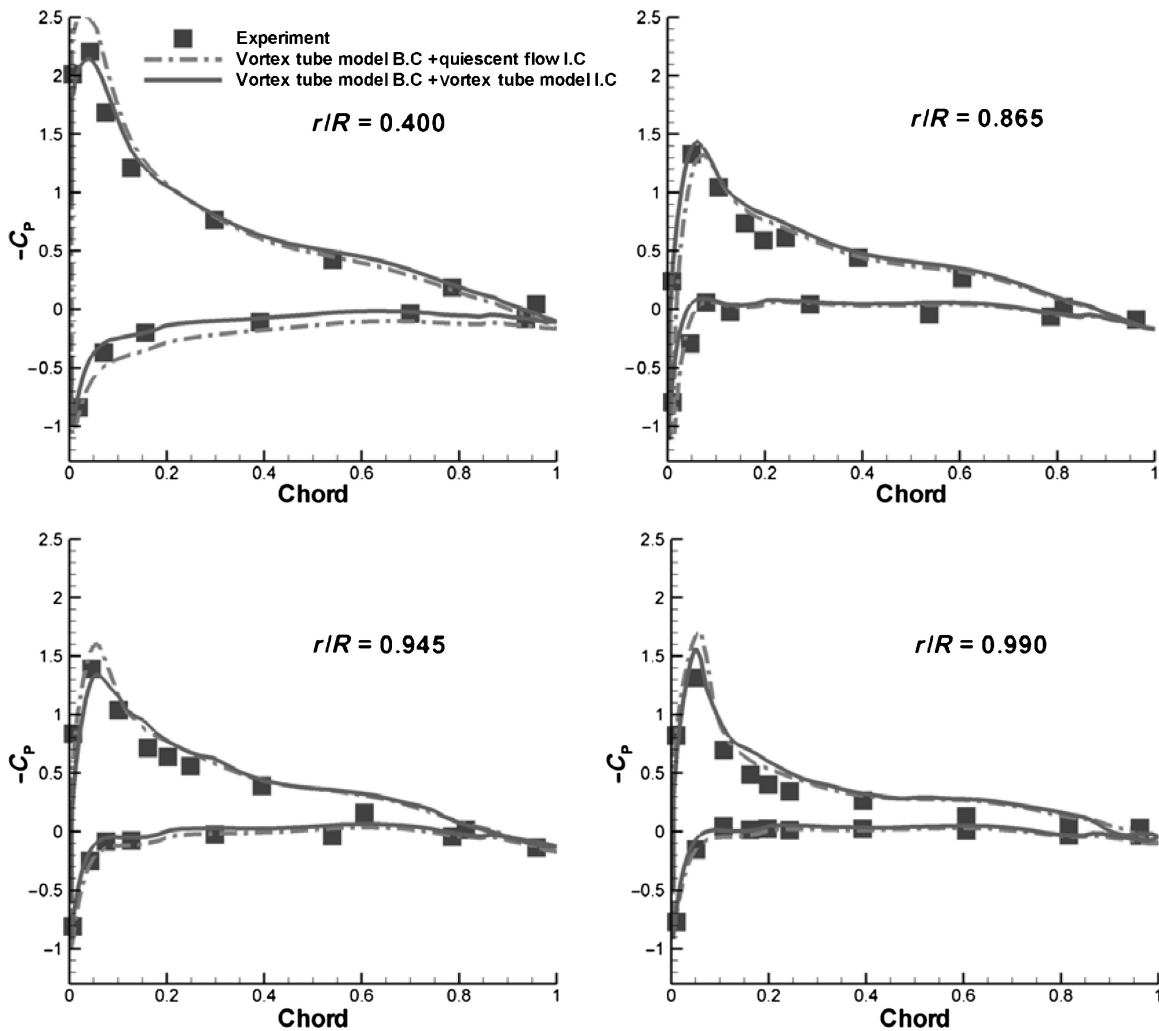


Fig. 9. Chordwise pressure distributions at selected radial station ($M_{tip} = 0.628$, $C_T = 0.00706$).

which require 90 h on 16 Intel 3.2 GHz processors to complete 60,000 iterations. The results of both far-field boundary conditions with the quiescent flow initial condition show similar convergence history at the early stage of computation. After six revolutions, they show a little difference. It is probable that the far-field boundary condition would have little effect on the initial computation before rotor wake is fully developed to reach the bottom far-field boundary. Thrust shows little change after 10 revolutions, but still slowly oscillates as iteration continues. Its variation is less than 3% of the thrust coefficient.

The results of both far-field boundary conditions with the quiescent flow initial condition show similar convergence history, which has steep increases of C_T at the early stage of computation like many previous hovering computations (Ref. 14). Since there is a quiescent flow field around the rotor at the start of numerical computation, there is no downwash through the rotor disk, causing a decrease of the effective angle of attack. As the iteration step continues, rotor blades generate the downwash through the rotor disk, and it reduces the effective angle of attack. Then computed thrust is decreased to the converged thrust. This means that the conventional initial condition requires more time to converge thrust. Moreover, a strong rotating flow, which is called the “starting vortex,” occurs in the computations. It slowly moves downward by downwash.

Thus, it requires additional iteration steps to eliminate this spurious rotating flow.

Instead of using the quiescent flow assumption, the initial condition using the truncated vortex tube model could accelerate the convergence, as shown in Fig. 6. The vortex tube induced flow fields of a hovering rotor are used for the initial condition as well as for the far-field boundary condition. Computation results of the truncated vortex tube boundary condition and initial condition shows almost same converged thrust and faster convergence. Downwash initially induced by the vortex tube is likely to reduce the effective angle of attack of the rotor blade. As a result, it would prevent the steep increase of the thrust at the initial stage of computation. It would also weaken the starting vortex. This will be dealt with more fully in the following rotor wake analysis. As a result, it requires only about five or six revolutions to obtain the converged solution.

Overall rotor performance

The results of overall thrust and power for the test case are shown in Fig. 7(a). The computed torque versus thrust of both boundary conditions shows good agreement with the experimental result. The initial condition

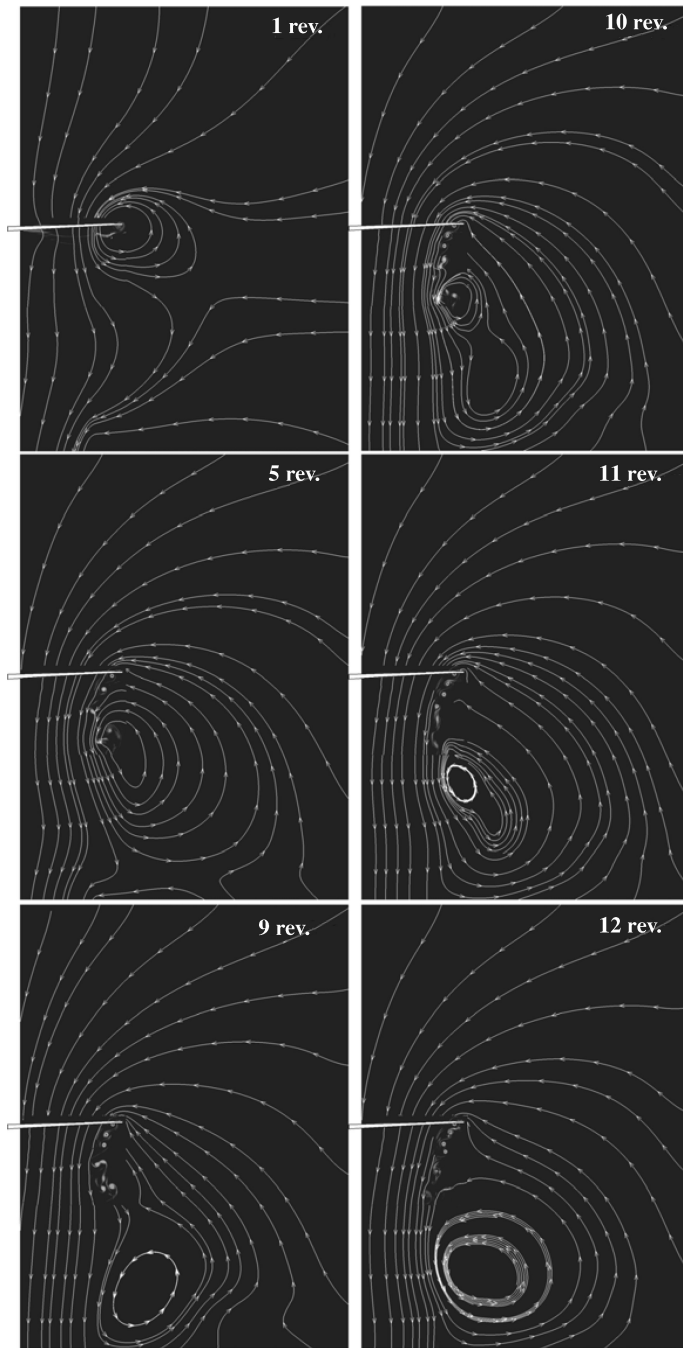
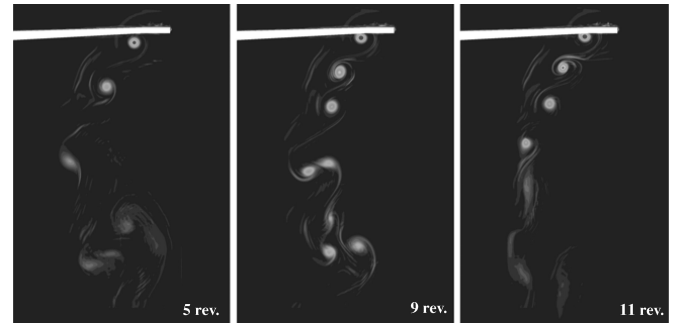


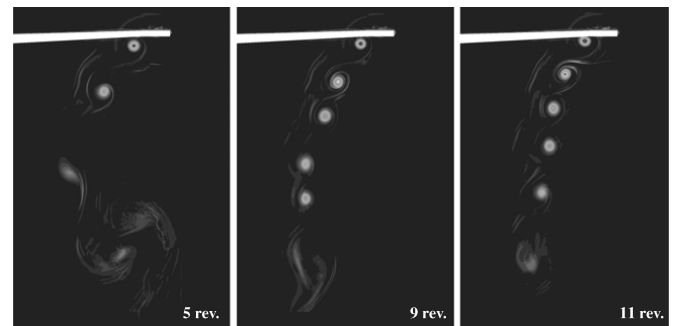
Fig. 10. Rotor wake growth in the source-sink model boundary condition with quiescent flow initial condition ($2R$ far-field boundary).

using the truncated vortex tube model also produces similar thrust and power curve. This initial condition shows slightly better accuracy in the prediction of low thrust level at $C_T = 0.004$ than the quiescent flow initial condition. A computed figure of merit plot generally agrees with the measured result, but shows a small underprediction of less than 5%, as shown in Fig. 7(b).

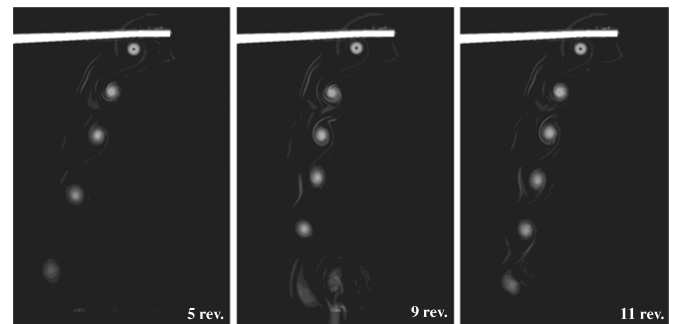
The computed spanwise thrust distributions are also compared with the experimental data for three different far-field boundary locations: $1.5R$, $2R$, and $3R$. The result of $5R$ boundary location is very similar to that of $3R$ boundary location. The computed results of both boundary conditions show reasonably good agreement with the experimental data



(a) Source-sink model boundary condition with quiescent flow initial condition



(b) Truncated vortex tube model boundary condition with quiescent flow initial condition



(c) Truncated vortex tube model condition with truncated vortex tube model initial condition

Fig. 11. Computed vorticity contour of rotor tip vortices on a cutting plane 0 deg behind the rotor blade ($2R$ far-field boundary).

except for the rotor tip, as shown in Fig. 8. Thrust is overpredicted near the rotor tip in both far-field boundary conditions with the quiescent flow initial condition. It is one of the chronic problems in the CFD analysis of the hovering rotor. These results are deeply concerned with the smaller vertical miss distance of the tip vortex below the rotor blade and the larger vortex core radius in computed results than in a real case (Ref. 14). It is very difficult to compute the exact location and core size of the tip vortex. Note that as the far-field boundary location becomes closer, the results of source-sink model show larger overpredictions than that of the vortex tube model. The truncated vortex tube model boundary condition slightly reduces the thrust overprediction and shows better correlation to the experimental data. Since all the cases are conducted at the same hovering condition, and near field grids have same grid resolution, the vortex core radius and strength would hardly change. Thus, the overprediction in these computations may mainly result from the small miss distance. The far-field boundary condition is likely to affect the miss distance and rotor wake geometry.

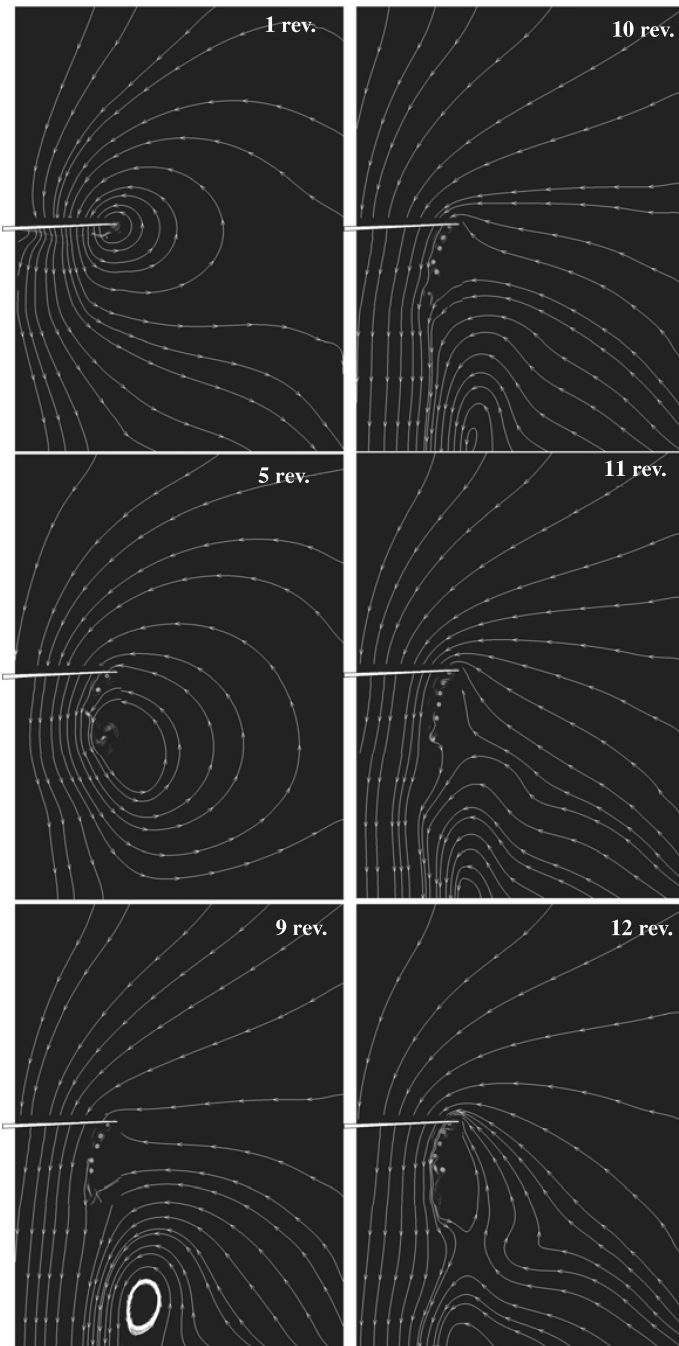


Fig. 12. Rotor wake growth in the truncated vortex tube model boundary condition with quiescent flow initial condition ($2R$ far-field boundary).

Another remarkable result is that the vortex tube model initial condition shows quite good predictions. The overprediction of thrust, observed in the case of the quiescent flow initial condition, is not observed for any of different far-field boundary locations. The result of the vortex tube model initial condition is unlikely to be affected significantly by the far-field boundary location.

The computed chordwise pressure distributions are also compared with the measured data at four radial locations, as shown in Fig. 9. The correlation looks quite good at each radial station. The small discrepancies at $r/R = 0.990$ is reflected in the C_T overprediction at the rotor tip, as shown in Fig. 8. Based on these results, the truncated vortex tube

model seems to be successfully adopted as the far-field boundary condition and initial condition for the hovering analysis. Furthermore, using the truncated vortex tube model for both boundary condition and initial condition shows the possibility of improvement on an accuracy of the solution as well as an efficiency of computation.

Effects on rotor wake development

An interesting question is why using the truncated vortex tube model provides such improvements in accuracy and convergence. It appears to be deeply concerned with a rotor flow field that the model generates. One possible cause is the differences in the inflow/outflow conditions at the bottom far-field boundary. Figure 10 shows streamlines and computed vorticity contour on a cutting plane located just behind rotor blade. The result using the source-sink boundary condition and the quiescent initial condition shows that the rotor induces a large-scale rotating flow outside the rotor wake, which is usually called the starting vortex. As rotor rotation continues, this rotating flow moves downward along the rotor downwash. It finally approaches the bottom inflow boundary after a few rotor revolutions. However, only the specified far-field boundary whose radius is $1.12R/\sqrt{2}$ allows outflow in the source-sink boundary condition. Inflow velocity toward the rotor hub is specified by Eq. (2) on the rest of the bottom boundary outside the circular outflow region. Thus, this spurious rotating flow cannot exit the bottom boundary, and it takes time until the rotating flow is completely dissipated, although it continues to become weaker and dissipated. If the CFD solver could be improved to be less dissipative, the effects of the starting vortex would have an even greater side effect. Moreover, the computation shows the formation and movement of the other large rotating flow outside the rotor wake tube after the starting vortex. During the rotor revolution, this rotating flow is repeatedly generated and moving downward along the rotor wake, and finally merging with the remnant of the former starting vortex, as shown in the snapshots of rotor flows from 9 to 12 revolutions in Fig. 10.

This is likely to have a negative effect on the prediction of rotor wake geometry. Such a rotating flow could become an obstacle that prevents tip vortices from moving downward. The distortion of rotor wake geometry is seen, as shown in Fig. 11(a). It could also reduce the miss distance, which results in the overprediction of a rotor tip thrust. Thus, it may require a rather large grid to prevent the effect of the distorted flow. Strawn and Djomehri (Ref. 14) showed that C_T and C_Q values show little change beyond $3R$ boundary location. We also observed that the effect of far-field boundary conditions is reduced beyond $3R$ boundary location. Although the prediction of overall rotor performance is not significantly affected by the far-field boundary condition or far-field location, tip vortices seem to be sensitive to the far-field boundary condition when the distance between the rotor and far-field boundary is relatively short.

In contrast to the source-sink boundary condition, the truncated vortex tube model boundary condition allows the starting vortex to go through the bottom boundary, as shown in Fig. 12. The vortex tube model boundary condition seems to minimize the effect of the starting vortex, because the rotating flow can pass the bottom boundary through the marginal outflow region, as shown in the snapshots from 9 to 12 revolutions in Fig. 12. Thus, the result of the vortex tube model boundary condition shows more stable wake structure, as shown in Fig. 11(b).

Figure 13 shows different rotor wake growth pattern for the truncated vortex tube model initial condition combined with the far-field boundary condition. As shown in the initial flow field of one revolution in Fig. 13, there is a large rotating flow outside the rotor wake, and strong downwash flow inside the rotor wake region, which corresponds to the inner side of the vortex tube. This downwash accelerates the rotating flow going out of the bottom boundary and also helps the formation of tip vortices and faster construction of the rotor wake structure than does the quiescent flow

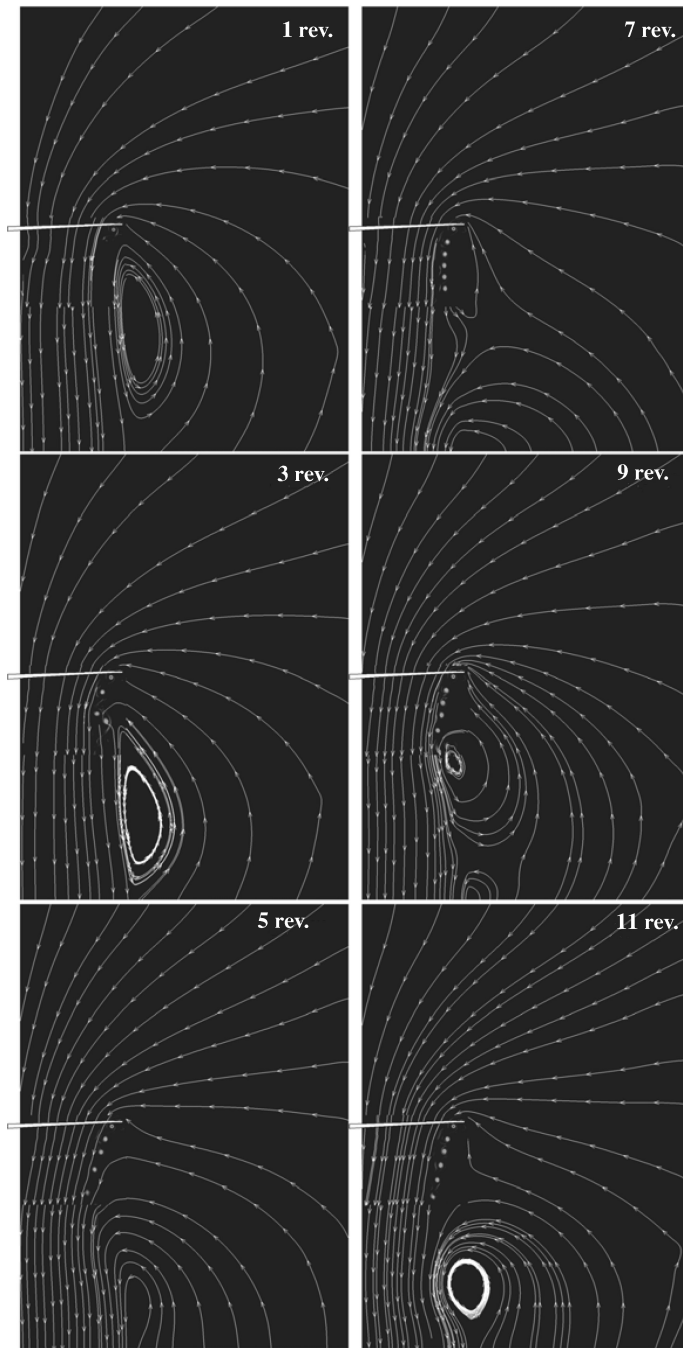


Fig. 13. Rotor wake growth in the truncated vortex tube model boundary condition with the truncated vortex tube model initial condition ($2R$ far-field boundary).

initial condition. It takes only five revolutions to form a stable wake structure for the hovering rotor, while nine revolutions is usually required with the quiescent initial condition, as shown in Fig. 11. These factors enable the fast convergence of the truncated vortex tube model initial condition.

Effects on rotor wake geometry

Another key difference between the two boundary conditions is a vertical miss distance between a rotor blade and the nearest tip vortex, which is generated by a preceding blade. This distance is a key parameter of rotor aerodynamics and acoustics. Figure 11 shows that the computed

preceding tip vortex passes under the rotor blade. All the results in Fig. 11 are computed with the $2R$ far-field boundary location. Its miss distance is only $0.17c$ in the source-sink model and $0.23c$ in the truncated vortex tube model, whereas the miss distance is about $0.4c$ in the experimental result (Ref. 14). Although the truncated vortex tube model boundary has slightly better accuracy than the source-sink model, the miss distance is still smaller than the measured one. In contrast, note that the miss distance is $0.42c$ in the result of the truncated vortex tube model initial condition, which agrees well with the measured value. This results in a good prediction of the rotor thrust. Rotor downwash induced by the vortex tube model may help the first generating tip vortex to move quickly downward at the initial stage of computation, whereas several rotor revolutions are required to generate sufficient downwash in the quiescent flow initial condition. In the five revolutions case shown in Fig. 11, the miss distance for the truncated vortex tube model initial condition is about $0.45c$, whereas $0.35c$ in the quiescent initial condition. Once tip vortices are fully developed, the downwash generated by tip vortices themselves would prevent the preceding tip vortex from approaching close to a blade.

Figure 14 shows the effect of the far-field boundary location on the rotor wake structure. If the far-field boundary is located beyond 3 blade

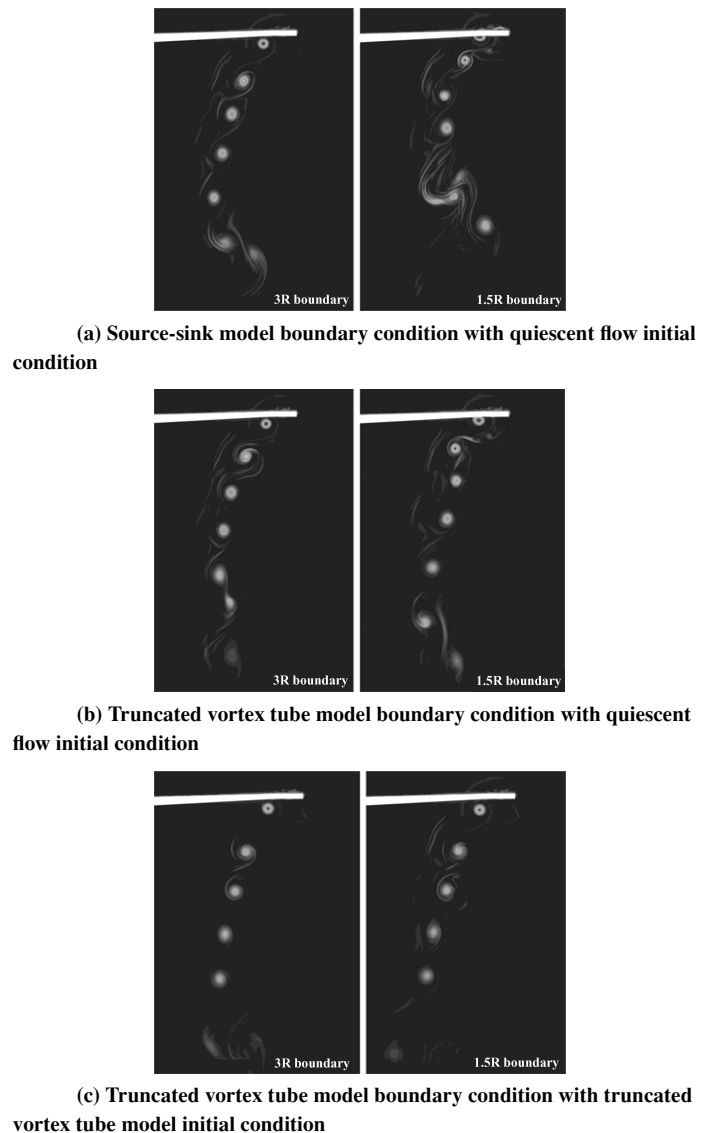


Fig. 14. Comparison of rotor wake according to the far-field boundary location.

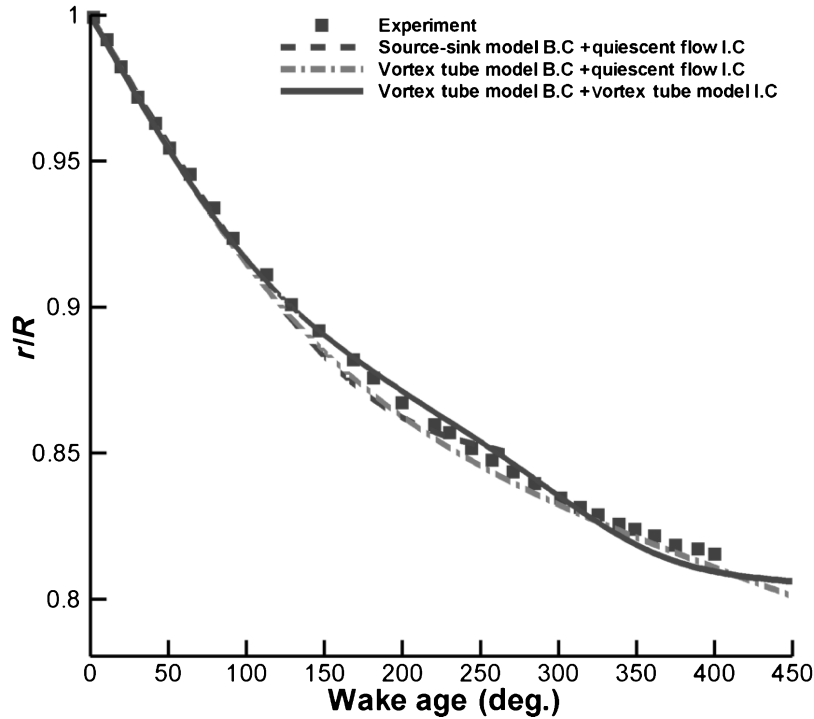


Fig. 15. Tip-vortex vertical descent ($M_{tip} = 0.628, C_T = 0.00706$).

radii from a rotor, it shows good agreement with the measured data. However, it requires much time to banish the starting vortex out of the computational domain, and there is still the thrust overprediction problem. In the $1.5R$ boundary case, a distorted and unstable wake structure is seen in the computation result of the source-sink boundary condition. Although the vortex tube model boundary condition would improve the hovering solution, it is not perfectly free from the effect of boundary and starting vortex. In general, as the far-field boundary location becomes

closer, the miss distance is likely to be decreased, resulting in the overprediction of the sectional thrust, such as the $1.5R$ boundary case in Fig. 8. However, the initial condition and the boundary condition, using the truncated vortex tube model, show good prediction of the rotor wake regardless of the far-field boundary location, as shown in Fig. 14(c).

Lorber et al. (Ref. 13) presented experimental measurements for the geometry of the rotor tip vortices. Figure 15 shows vertical tip-vortex descent, and Fig. 16 shows tip-vortex radial contraction. The center of

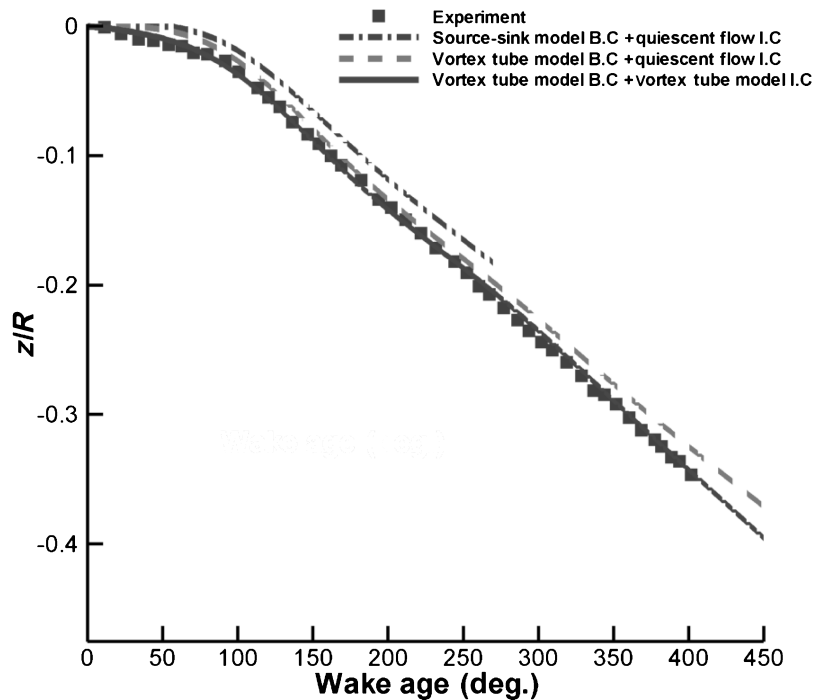


Fig. 16. Tip-vortex radial contraction ($M_{tip} = 0.628, C_T = 0.00706$).

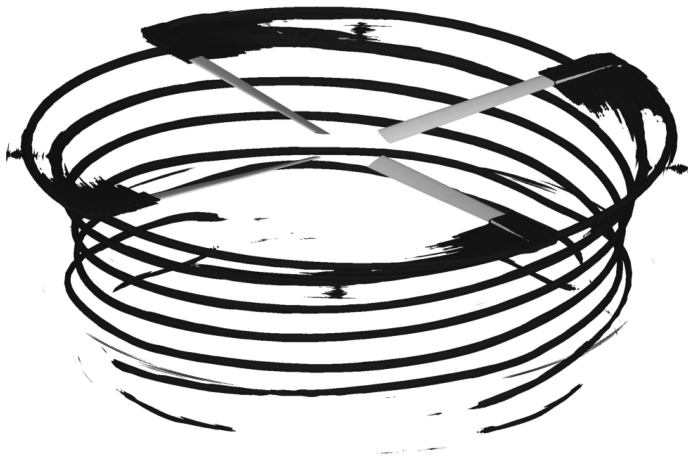


Fig. 17. Isovorticity surfaces of hovering rotor tip vortices (vorticity = 0.35, the truncated vortex tube model B.C and truncated vortex tube model I.C).

tip vortex is calculated by finding local maxima in vorticity magnitude in each azimuthal angle. The vortex structure is very unsteady system. Thus, both the experimental results and the computed results contain a fair amount of uncertainty (Ref. 14). The computed rotor wake geometry using the truncated vortex tube model boundary condition shows better accuracy than that of the source-sink boundary condition. The three-dimensional structure of rotor wake can be clearly seen in Fig. 17, which is the isovorticity contour of the vortex tube model case.

Climbing flight

The application of the truncated vortex tube model is easily extended to the climbing/descending flight. The height of the truncated vortex tube is dependent on the vertical velocity, and it is determined by an empirical formula (Ref. 17). McAlister et al. (Ref. 27) presented experimental measurements for the rotor performance and tip vortex in various climbing flight conditions. The model used in this experiment was a 1/7-scale of the AH-1/OLS rotor, which consists of two blades, each with a chord of 4.09 inches and a span of 37.7 inches measured from the axis of rotation to the blade tip. The collective pitch angle and the climb velocity were the only variables in this test. The calculations were performed for three pitch angles: 7, 9, and 11 deg. The climb velocities, which were normalized by the rotor tip velocity, were adjusted from 0 to 0.03. Tip Mach number was $M_{tip} = 0.26$, and the Reynolds number based on the tip chord length was $Re = 0.6 \times 10^6$.

Computations using the truncated vortex tube model were performed for the comparison of the rotor performance in climbing flight. The initial condition using the truncated vortex tube model was also used to accelerate convergence. Figure 18 presents a convergence plot for a climbing rotor. The computation using the quiescent initial condition and the truncated vortex tube model boundary condition does not completely converge to steady-state solution, but slowly oscillates as iteration continues. Its variation is less than 2% of the thrust coefficient. In contrast, initialization using the truncated vortex tube model reduces the oscillation of the thrust, and it also reduced the computational time for the convergence of solution by half. To set the initial value using the truncated vortex tube model is also effective in obtaining a more accurate performance prediction of the climbing rotor.

The figure of merit versus the vertical velocity for the test case is shown in Fig. 19. The prediction for the pitch angle, $\theta = 7^\circ$, shows a little larger discrepancy. However, all these discrepancies are less than 5%

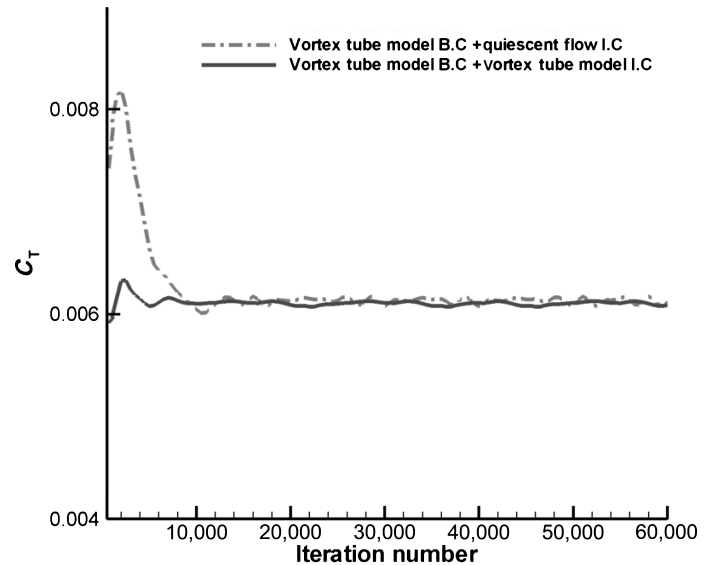


Fig. 18. Thrust convergence history for a climbing rotor.

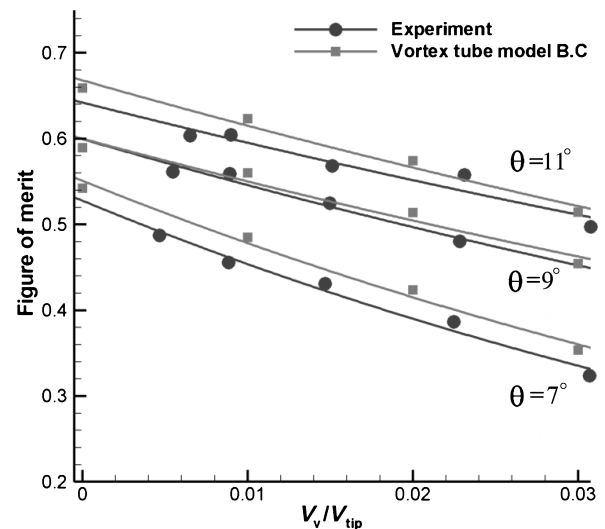


Fig. 19. Rotor performance for various climb rates and collective pitch angles.

of the figure of merit. It generally shows good agreement with the experimental result for the specified range of climbing velocity. In particular, the figure of merit decreases almost linearly as the climb velocity increases. Figure 20 clearly shows another correlation between climbing velocity and performance. As the normalized climb velocity increases from 0.01 to 0.03, the spanwise thrust distribution is shifted vertically downward. This shift is very similar to the case of decrease in the collective pitch angle. It may result from the decrease of the effective angle of attack, which is caused by the effect of vertical inflow. Since the tip vortex quickly convects downward due to the vertical inflow, there is no thrust overshoot at the rotor tip, which is generally seen in hovering computations.

Descending flight

Numerical simulations were performed for a model helicopter rotor in descending flight, which was tested by Washizu and Azuma (Refs. 28,29). The model rotor has three blades, with diameter of 1100 mm, and chord of 33 mm. The blade has a linear twist of $8^\circ 20'$ from root to tip.

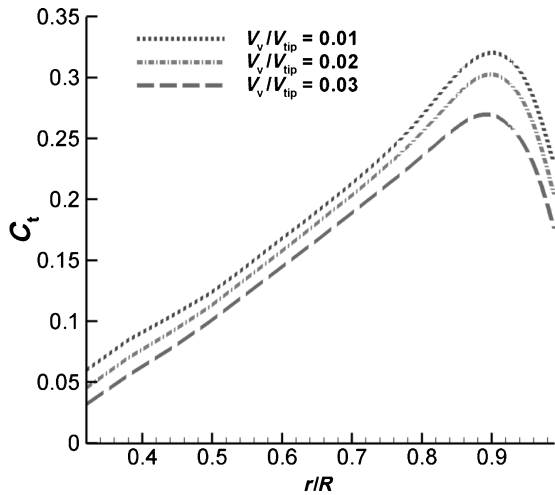


Fig. 20. Spanwise thrust distribution for various climb rates (collective pitch angle, $\theta = 7^\circ$).

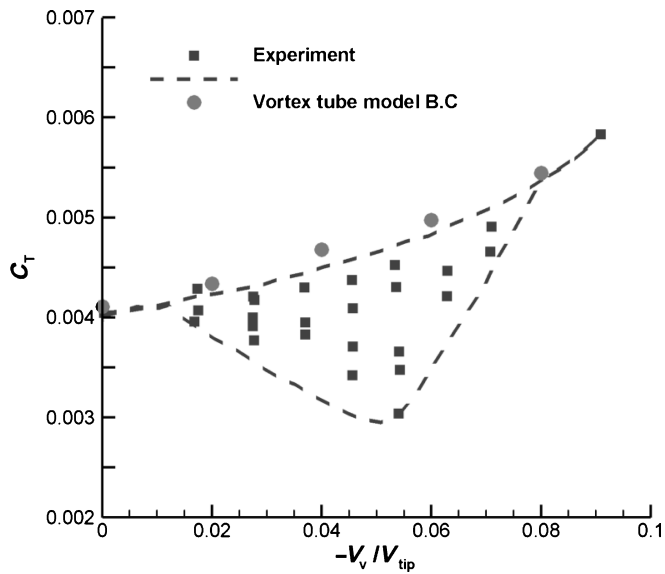


Fig. 21. Thrust for various rates of descent (collective pitch angle, $\theta = 8^\circ$).

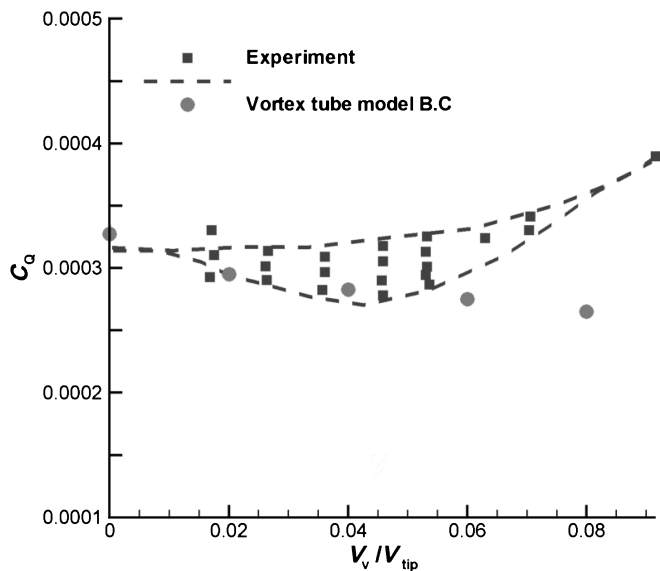
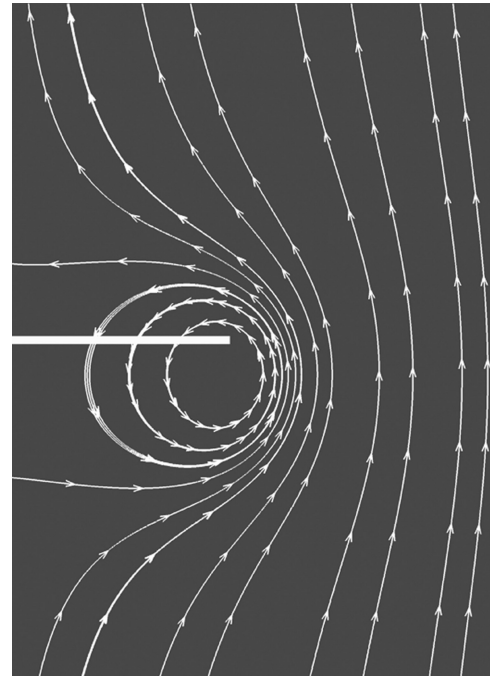
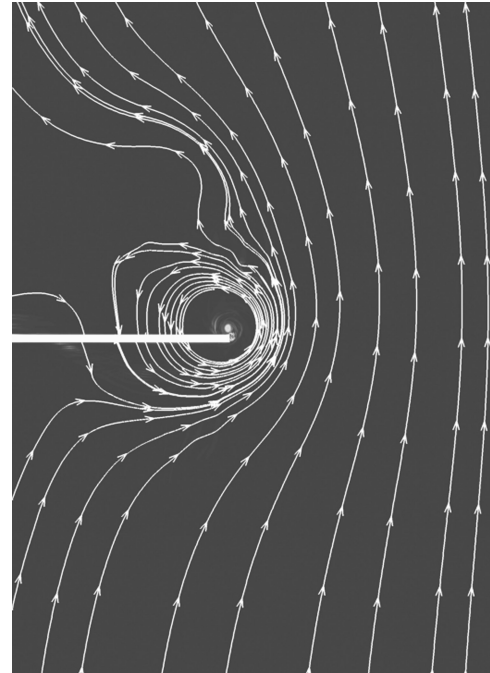


Fig. 22. Power for various rates of descent.



(a) Analytic result using vortex tube model



(b) CFD result using vortex tube model boundary condition

Fig. 23. Computed streamline for the descending rotor ($V_{int}/V_{tip} = -0.06$).

Experimental measurements for the rotor performance were presented for various descent conditions. The presence of severe thrust fluctuations was observed in the study, as shown in Figs. 21 and 22. For this reason, approximate curve fits for the experimental result were provided; these are shown as a dotted line in the figure. The computed results are presented for the various descent velocities normalized by the rotor tip velocity at $V_V/V_{Tip} = 0.00, -0.02, -0.04, -0.06,$ and -0.08 . The collective pitch angle is set to 8 deg. The predicted thrust is slightly higher than the experimental data. The prediction shows a good agreement with the curve fit for the maximum value of the experimental result. No severe fluctuation of the thrust was observed in the computed result.

Figure 22 presents computed and experimental power curves. Again, the predictions are in quite good agreement with the experimental power for the region of low descent velocity, but the computed power becomes smaller than the measured power, as the normalized descent velocity is increased above 0.06. In general, a descending rotor gets into the vortex ring state, when the descent velocity approaches the induced velocity in hovering state. The rate of descent for the vortex ring state is approximately $V_V/V_{Tip} = -0.05$ in this case. The vortex ring state is very unsteady, possibly resulting in the discrepancies between the computed and experimental results. Figure 23 shows the vorticity contour and streamline for the descending velocity, $V_V/V_{Tip} = -0.06$.

As the numerical methods in this study are based on the quasi-steady state assumptions when using the source term formulation (Ref. 20), it has a limitation in dealing with highly unsteady flow for the vertical flight. Nevertheless, overall results show good correlations with the experimental data of vertical flight. Thus, it is expected that the application of the truncated vortex tube model will be easily extended to the fully unsteady solver and will show better accuracy in the analysis of highly unsteady flow, such as the vortex ring state. More detailed analysis for vertical flight will be performed in future studies.

Conclusions

This research has been designed to investigate a new boundary condition and initial condition based on the truncated vortex tube model for the helicopter rotor analysis. The conventional source-sink model has limitations in predicting the rotor wake and is limited in application to hover. To overcome this problem, this study has focused on the truncated vortex tube model, which was devised for the analytic computation of the induced velocity in the vertical flight. The formulation was easily implemented in the HeliNA solver.

Applying this model shows two possibilities for improving the CFD analysis of helicopter rotor. One possibility is the application to the far-field boundary condition. The induced velocity values calculated from the truncated vortex tube model were used to specify the far-field boundary condition for vertical flight as well as hovering flight. Computation using this model showed good agreements with the experimental performance data and better accuracy in the rotor wake prediction.

The other possibility is the application of the initial condition. The vortex tube model, can easily generate the mean flow field based on the predicted overall thrust and vertical velocity. Although the computed flow field is relatively simple, the simulated and observed flow patterns are very similar in the various flight conditions. Thus, it is advantageous to adopt the induced flow field values instead of quiescent flow fields as an initial condition. The numerical analysis indicates that use of the truncated vortex tube model as an initial condition tends to reduce convergence time by half and to give more stable solutions without losing the accuracy of performance prediction.

In conclusion, the overall results show that the new far-field boundary condition and initial condition, using the truncated vortex tube model,

can be a useful tool as an alternative to the conventional method for the improved numerical analysis of helicopter rotors.

Acknowledgments

This work is outcome of the fostering project of the Best Lab supported financially by the Ministry of Commerce, Industry and Energy (MOCIE) in Korea. This study has been supported by the KARI under KHP Dual-Use Component Development Program funded by the MOCIE.

References

- ¹Kang, H. J., and Kwon, O. J., "Unstructured Mesh Navier–Stokes Calculations of the Flow Field of a Helicopter Rotor in Hover," *Journal of the American Helicopter Society*, Vol. 47, (2), April 2002, pp. 90–99.
- ²Boniface, J. C., and Pahlke, K., "Calculations of Multi-bladed Rotors in Forward Flight Using 3D Euler Methods of DLR and ONERA," 22nd European Rotorcraft Forum, Brighton, UK, September 17–19, 1996.
- ³Park, Y., Nam, H., and Kwon, O., "Simulation of Unsteady Rotor–Fuselage Interactions Using Unstructured Adaptive Meshes," American Helicopter Society 59th Annual Forum Proceedings, Phoenix, AZ, May 6–8, 2003.
- ⁴Hariharan, N., and Sankar, L. N., "Application of ENO Schemes to Rotary Wing Problems," Paper AIAA 1995-1892, 13th AIAA Applied Aerodynamics Conference, San Diego, CA, June 19–22, 1995.
- ⁵Jiang, G. S., and Shu, C. W., "Efficient Implementation of Weighted ENO Schemes," *Journal of Computational Physics*, Vol. 126, 1996, pp. 202–228.
- ⁶Usta, E., Wake, B. E., Egolf, T. A., and Sankar, L. N., "Application of a Symmetric Total Variation Diminishing Scheme to Aerodynamics and Aeroacoustics of Rotors," American Helicopter Society 57th Annual Forum Proceedings, Washington DC, May 9–11, 2001.
- ⁷Wenren, Y., and Steinhoff, J., "Application of Vorticity Confinement to the Prediction of the Wake of Helicopter Rotors and Complex Bodies," AIAA 99-3200, 17th Applied Aerodynamics Conference, Norfolk, VA, June 28–July 1, 1999.
- ⁸Berkman, M. E., Sankar, L. N., Berezin, C. R., and Torok, M. S., "Navier–Stokes/Full Potential/Free-Wake Method for Rotor Flows," *Journal of Aircraft*, Vol. 34, (5), 1997, pp. 635–640.
- ⁹Brown, R. E., "Rotor Wake Modeling for Flight Dynamic Simulation of Helicopters," *AIAA Journal*, Vol. 38, (1), 2000, pp. 57–63.
- ¹⁰Srinivasan, G. R., Baeder, J. D., Obayashi, S., and McCroskey, W. J., "Flow Field of a Lifting Rotor in Hover: A Navier–Stokes Simulation," *AIAA Journal*, Vol. 30, (10), 1992, pp. 2371–2378.
- ¹¹Srinivasan, G. R., Raghavan, V., Duque, E. P. N., and McCroskey, W. J., "Flow Field Analysis of Modern Helicopter Rotors in Hover by Navier–Stokes Method," *Journal of the American Helicopter Society*, Vol. 38, (3), July 1993, pp. 3–13.
- ¹²Brian E. W., and Baeder J. D., "Evaluation of a Navier–Stokes Analysis Method for Hover Performance Prediction," *Journal of the American Helicopter Society*, Vol. 41, (1), January 1996, pp. 1–17.
- ¹³Lorber, P. F., Stauter, R. C., and Landgrebe, A. J., "A Comprehensive Hover Test of the Airloads and Airflow of an Extensively Instrumented Model Helicopter Rotor," American Helicopter Society 45th Annual Forum Proceedings, Boston, MA, May 22–24, 1989, pp. 281–295.
- ¹⁴Strawn, R. C., and Djomehri, M. J., "Computational Modeling of Hovering Rotor and Wake Aerodynamics," *Journal of Aircraft*, Vol. 39, (5), September–October 2002, pp. 786–793.
- ¹⁵Beaumier, P., Chelli, E., and Pahlke, K., "Navier–Stokes Prediction of Helicopter Rotor Performance in Hover Including Aero-Elastic Effects," American Helicopter Society 56th Annual Forum Proceedings, Virginia Beach, VA, May 2–4, 2000.

¹⁶Horlock, J. H., *Actuator Disk Theory*, McGraw-Hill, New York, NY, 1978.

¹⁷Wang, S. C., "Analytical Approach to the Induced Flow of a Helicopter Rotor in Vertical Descent," *Journal of the American Helicopter Society*, Vol. 35, (1), January 1990, pp. 92–98.

¹⁸Perry, F. J., Chan, W. Y. F., Simons, I. A., Brown, R. E., Ahlin, G. A., Khelifa, B. M., and Newman, S. J. "Modeling the Mean Flow through a Rotor in Axial Flight Including Vortex Ring Conditions," *Journal of the American Helicopter Society*, Vol. 52, (3), July 2007, pp. 224–238.

¹⁹Yoon, S., and Jameson, A., "Lower-Upper Symmetric-Gauss-Seidel Method for the Euler and Navier–Stokes Equations," *AIAA Journal*, Vol. 26, (9), September 1988, pp. 1025–1026.

²⁰Chen, C. L., McCroskey, W. J., and Obayashi, S., "Numerical Solutions of Forward-Flight Rotor Flows Using an Upwind Method," *Journal of Aircraft*, Vol. 28, (6), 1991, pp. 374–380.

²¹Peters, D. A., and Chen, S. Y., "Momentum Theory, Dynamic Inflow and the Vortex-Ring State," *Journal of the American Helicopter Society*, Vol. 27, (3), July 1982, pp. 18–24.

²²Stack, J., "Experimental Investigation of Rotor Vortex Wakes in Descent," 42nd AIAA Aerospace Sciences Meeting Proceedings, Reno, NV, January 5–8, 2004.

²³Osvaldo, M. Q., "Rotor Wake Investigation Using the Smoke Flow Visualization Technique," M.Sc. Thesis, Department of Aeronautical Engineering, University of Sydney, Sydney, Australia, March 1993.

²⁴Bhagwat, M. J., and Leishman, J. G., "On the Aerodynamic Stability of Helicopter Rotor Wakes," American Helicopter Society 56th Annual Forum Proceedings, Virginia Beach, VA, May 2–4, 2000.

²⁵Chung, K. H., Na, S. U., Jeon, W. H., and Lee, D. J., "A Study on Rotor Tip-Vortex Roll-Up Phenomenon by Using Time-Marching Free-Wake Method," American Helicopter Society 56th Annual Forum Proceedings, Virginia Beach, VA, May 2–4, 2000.

²⁶Brown, R. E., Line, A. J., "Efficient High-Resolution Wake Modelling Using the Vorticity Transport Equation," *AIAA Journal*, Vol. 43, (7), 2005, pp. 1434–1443.

²⁷McAlister, K. W., Huang, S. S., and Abrego, A. I., "A Model Rotor in Axial Flight," NASA TM-2001-210925, June 2001.

²⁸Washizu, K., Azuma, A., Kôo, J., and Oka, T., "Experiments on a Model Helicopter Rotor Operating in the Vortex Ring State," *Journal of Aircraft*, Vol. 3, (3), 1966, pp. 225–230.

²⁹Azuma, A., and Obata, A., "Induced Flow Variation of the Helicopter Rotor Operating in the Vortex Ring State," *Journal of Aircraft*, Vol. 5, (4), 1968, pp. 381–386.